

# The Fast Stochastic Matching Pursuit for Neutrino and Dark Matter Experiments

Yuyi Wang<sup>1,2,3</sup>, Aiqiang Zhang<sup>1,2,3</sup>, Yiyang Wu<sup>1,2,3</sup>, Benda Xu<sup>1,2,3\*</sup>, Jiajie Chen<sup>4</sup>, Zhe Wang<sup>1,2,3</sup>, Shaomin Chen<sup>1,2,3</sup>

<sup>1</sup> Department of Engineering Physics, Tsinghua University, Beijing,100084,China.

<sup>2</sup> Center for High Energy Physics, Tsinghua University, Beijing,100084,China.

<sup>3</sup> Key Laboratory of Particle & Radiation Imaging (Tsinghua University), Ministry of Education, China.

<sup>4</sup> Department of Computer Science and Technology, Tsinghua University, Beijing,100084,China.

\*Corresponding author(s). E-mail(s): [orv@tsinghua.edu.cn](mailto:orv@tsinghua.edu.cn);

## Abstract

Photomultiplier tubes (PMT) are widely deployed at neutrino and dark matter experiments for photon counting. When multiple photons hit a PMT consecutively, their photo-electron (PE) pulses pile up to hinder the precise measurements of the count and timings. We introduce Fast Stochastic Matching Pursuit (FSMP) to analyze the PMT signal waveforms into individual PEs with the strategy of reversible-jump Markov-chain Monte Carlo. We demonstrate that FSMP improves the energy and time resolution of PMT-based experiments, gains acceleration on GPUs and is extensible to microchannel-plate (MCP) PMTs with jumbo-charge outputs. In the condition of our laboratory characterization of 8-inch MCP-PMTs, FSMP improves the energy resolution by up to 12% from the long-serving method of waveform integration.

**Keywords:** waveform analysis, MCP-PMT, energy resolution, time resolution, GPU acceleration

# 1 Introduction

Large detectors with photomultiplier tubes (PMT) around are set up for the invisible, enigmatic, challenging-to-detect neutrinos and dark matters. The electronic systems read photon-induced pulses embedded in the time series of PMTs voltage outputs, or *waveforms*. Experiments deploying full waveform readout includes KamLAND [1], Borexino [2], JUNO [3], Jinping Neutrino Experiment (JNE) [4–6], as well as XMASS [7], PandaX-4T [8] and LUX-ZEPLIN [9].

To reconstruct the energy and time of the events from the waveforms, a common method is to integrate the waveform to get the *charge* [10] as a predictor of visible energy, and to locate the peaks of the waveforms measuring the 10%-rising-edge [11] as photoelectron (PE) times. More sophisticated approaches use fitting or deconvolution [10, 12] based on empirical single PE templates to obtain the charge and PE arrival times together.

When the time difference of two PEs is small, their waveforms *pile up* [13], preventing reliable counting of the PEs. Therefore, a posterior distribution of PEs in the Bayesian sense is necessary to properly represent the uncertainty of the inference from the waveforms. For a complete Bayesian solution, we face a hierarchical, discrete-continuous and trans-dimensional challenge. *Fast Stochastic Matching Pursuit* (FSMP) is a fast and flexible algorithm to utilize all information from the waveforms. It was introduced in our previous publication of Xu et al. [12] with a comprehensive comparison of all the waveform analysis methods. It was then utilized to analyze a variety of PMTs and most notably adopted to the new microchannel-plate (MCP) PMTs [11] showing outstanding performance. To facilitate its understanding and application, we present the principles and details of FSMP in this article.

Without loss of generality, we use JNE [6], a liquid-scintillator (LS) detector under construction, as our discussion context. Section 2 gives an introduction of our methodology to tackle the challenge of PE pile-up. Performance evaluation based on simulation in Section 3 demonstrates the GPU acceleration and substantial improvement in energy resolution. Application of FSMP to experimental data in Section 4 provides a firm analysis basis to unveil the physics process inside MCP-PMTs.

## 2 Methodology

In FSMP, we use Gibbs Markov chain Monte-Carlo (MCMC), mixed with reversible jump MCMC (RJMCMC) [14] and Metropolis-Hastings construction [15] to analyze the waveforms by sampling from the posterior distribution of PE sequences. We adopt the notations by Xu et al. [12] and review only the essential definitions with an emphasis on the new MCP-PMTs.

### 2.1 Physical process

After a scintillator photon is emitted in an event and comes into the PMT, it hits some PEs out. The number of PEs  $N$  follows Poisson distribution [16, 17], with expectation  $\mu$ . The expectation of this Poisson process is a function of time, also known as

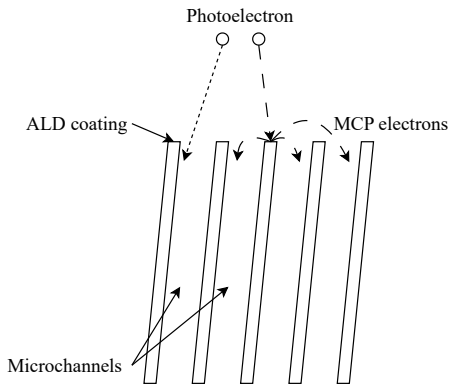
light curve:  $\mu\phi(t - t_0)$ , where  $\phi(t)$  is a normalized function, and  $t_0$  is a time offset. Lombardi [18] gives a method to calibrate light curve in LS.

A dynode PMT multiplies the electrons [19] on each of its many dynodes and collects them on the anode to produce a signal. Define the charge of a single PE as  $q$ , following normal distribution  $\mathcal{N}(\mu_q, \sigma_q)$  [20]. Considering that  $N$  follows Poisson distribution  $\pi(\mu)$ , the charge distribution of waveforms is a compound Poisson-Gaussian distribution.

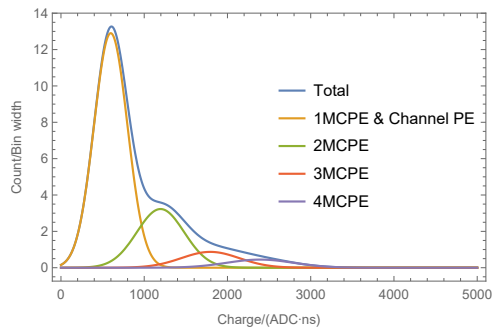
The dynodes may be replaced by MCP. The microchannels are atomic layer deposition (ALD) coated to improve the lifetime [21] and collection efficiency [22] but introduces *jumbo charges* [11]. In an MCP-PMT shown in Fig. 1a, there are two kinds of PE [23]. A PE may shoot directly into the microchannel and get multiplied, or hit on the ALD coating of the MCP upper surface. The latter produces multiple secondary electrons that we call *MCPes*. Here we define the case that PEs shot into the channel equal to the case that MCPes is 1. Define the MCPe count for one PE as  $e \in E$ , and generally  $E = \mathbb{Z}_+$ , while we choose  $E = \{1, 2, 3, 4\}$  to make calculation simpler. In that way, the charge model of single PE inside the MCP-PMT is constructed by a mixture of normal distributions [24]. For one PE, define the probability of MCPe  $e$  as  $G(e)$ , and the charge model is like

$$\sum_{e \in E} G(e) f_{\mathcal{N}}(eq, \sqrt{e}\sigma_q) \quad (1)$$

$G(e), q, \sigma_q$  are the input parameters of FSMP. Fig. 1b shows a sketch of the charge distribution in this model.



(a) A sketch of MCP and MCPes.



(b) A sketch of the charge model of an MCP-PMT. It is not normalized, because the vertical axis represents the number of waveforms.

**Fig. 1:** Sketches of MCP, MCPe, and MCP-PMT charge model.

If there are no photons coming into a PMT, the electronics should read out *electronic noises* [25]. The average of noise is the *baseline* of a PMT [24, 26]. When electrons hit the anode, the voltage of the anode decreases, and the PMT produces a negative pulse [27]. To analyze the waveform, integrate it to calculate charge [25]. The dimension of waveform charge is voltage multiplied by time, proportional to the electric charge accumulated on the anode. This article uses the ADC as the unit of voltage, and nanosecond as the unit of time. The unit of the charge is ADC·ns.

When only one PE produced in the PMT and gets multiplied, the produced waveform is alike [27]. Define such single electron response (SER) of a PMT as  $V_{\text{PE}}(t) = q\tilde{V}_{\text{PE}}(t)$ , where  $q$  is the single PE charge, and  $\tilde{V}$  is the normalized SER. The single PE charge follows normal distribution:  $q \sim \mathcal{N}(\mu_q, \sigma_q)$ . With SER and the electronic noise  $\epsilon$ , the final waveform  $w$  of a single PE is  $w(t) = q\tilde{V}_{\text{PE}}(t) + \epsilon$ .

## 2.2 Bayesian Inference

Let the light curve in Section 2.1 be  $\mu\phi(t - t_0)$  while  $t_0$  be the time of event. Define the PE sequence  $\mathbf{z} = \{t_1, t_2, \dots, t_N\} \in T^N$  as the time of each PE, the number of PEs as  $N$ , and the waveform as  $\mathbf{w}$ . With Bayesian theory [28], we can write down

$$p(\mathbf{z}, t_0 | \mathbf{w}) = \frac{p(\mathbf{w} | \mathbf{z}, t_0)p(\mathbf{z}, t_0)}{p(\mathbf{w})} \quad (2)$$

For a specific waveform,  $p(\mathbf{w})$  is a constant.  $p(\mathbf{z}, t_0)$  is the prior, and  $p(\mathbf{z}, t_0 | \mathbf{w})$  is the posterior. However, we do not know the true  $\mu$  and the true prior  $p(\mathbf{z}, t_0) = p(\mathbf{z} | \mu, t_0)p(t_0)$ , where  $p(\mathbf{z} | \mu, t_0)$  is defined in Section A.1 and  $p(t_0)$  is the  $t_0$  prior. Therefore, we guess a value  $\mu_0$  close to the true  $\mu$  yielding

$$p(\mathbf{z}, t_0 | \mathbf{w}) = \frac{p(\mathbf{w} | \mathbf{z}, t_0)p(\mathbf{z} | \mu_0, t_0)p(t_0)}{p(\mathbf{w})} \quad (3)$$

Section 3.3 gives an example to construct a distribution of  $\mu_0$  to cover the truth, and Section 4 uses deconvolution result as  $\mu_0$ .

It is important to choose a well-formed prior, to make the posterior unbiased. We choose a prior close to the reality: the light curve with  $\mu_0$ , while  $\mu_0$  is obtained from the deconvolution in Section 2.5. As for the  $t_0$  prior  $p(t_0)$ , different trigger system may follow different  $p(t_0)$ . Section 3 gives an example of a uniform prior, for both simulation and analysis.

The posterior  $p(\mathbf{z}, t_0 | \mathbf{w})$  is still hard to calculate. Gibbs MCMC [29] is suitable to sample  $\mathbf{z}$  and  $t_0$  from the conditional probabilities. To sample  $\mathbf{z}$  and  $t_0$ , Metropolis-Hastings MCMC [15] is chosen for both. The number of PEs is also unknown, so we need RJMCMC [14], a variant dimensional Metropolis-Hastings MCMC. In the Gibbs MCMC,  $t_0$  is sampled before  $\mathbf{z}$ . Therefore,  $t_{0,i+1}$  is sampled from  $p(t_{0,i+1} | \mathbf{z}_i)$ , and  $\mathbf{z}_{i+1}$  is sampled from  $p(\mathbf{z}_{i+1} | \mathbf{w}, t_{0,i+1})$ .

## 2.3 Sampling

Sampling of  $t_0$  is done by using Metropolis-Hastings with the acceptance:

$$\min \left\{ 1, \frac{p(\mathbf{z}_i | \mu_0, t'_{0,i+1})}{p(\mathbf{z}_i | \mu_0, t_{0,i})} \right\} \quad (4)$$

We accept a jump with the calculated acceptance, the possibility to accept the jump. The new sample will be recorded if the jump is accepted. Otherwise, record the previous sample. The prime in  $t'_{0,i+1}$  means the proposed value is waiting for judgement of accept or reject.

Sampling  $\mathbf{z}$  is done by RJMCMC, also with acceptances for each kind of jumps. Denote the length of  $\mathbf{z}_i$  as  $N_i$ , and define the jumps: birth, death, and update in Fig. 2. All jumps are reversible: birth jump is the reverse of death jump, and update jump is the reverse of itself.

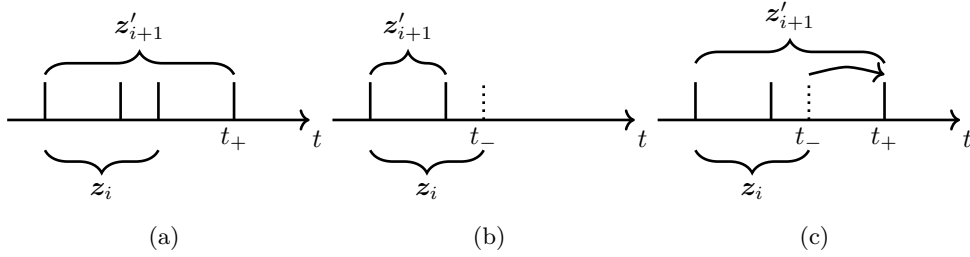


**Fig. 2:** Sketch of 3 jumps in RJMCMC. (a) Birth jump: the possibility of birth jump is  $h(t_+)$ . The possibility of the reverse jump is  $\frac{1}{N'_{i+1}}$ . (b) Death jump: the possibility of death jump is  $\frac{1}{N_i}$ . The possibility of the reverse jump is  $h(t_-)$ . (c) Update jump: the hit time  $t_-$  of one PE is updated to  $t_+ = t_- + \Delta t$ .

In the *birth jump* shown in Fig. 2a, a new PE  $t_+$  is appended to the sequence  $\mathbf{z}_i$ . Therefore,  $N'_{i+1} = N_i + 1$ , and  $\mathbf{z}'_{i+1} = \mathbf{z}_i \cup \{t_+\}$ . The distribution of  $t_+$  is the proposal  $h(t)dt$  introduced in Section 2.5. The acceptance is

$$\min \left\{ 1, \frac{p(\mathbf{z}'_{i+1} | \mu_0, t_{0,i+1}) \frac{1}{N'_{i+1}}}{p(\mathbf{z}_i | \mu_0, t_{0,i+1}) h(t_+)} \right\} \quad (5)$$

In the *death jump* shown in Fig. 2b, a PE  $t_-$  is removed in equal probability from the sequence  $\mathbf{z}_i$ . Therefore,  $N'_{i+1} = N_i - 1$ , and  $\mathbf{z}'_{i+1} = \mathbf{z}_i \setminus \{t_-\}$ . The acceptance is

$$\min \left\{ 1, \frac{p(\mathbf{z}'_{i+1} | \mu_0, t_{0,i+1}) h(t_-)}{p(\mathbf{z}_i | \mu_0, t_{0,i+1}) \frac{1}{N_i}} \right\} \quad (6)$$

In the *update jump* shown in Fig. 2c, a PE is moved from  $t_-$  to  $t_+ = t_- + \Delta t$ , and  $\Delta t$  follows a symmetry distribution  $\mathcal{N}(0, 1)$ . Therefore,  $N'_{i+1} = N_i$ , and  $\mathbf{z}'_{i+1} =$

$\mathbf{z}_i \setminus \{t_-\} \cup \{t_+\}$ . The acceptance is

$$\min \left\{ 1, \frac{p(\mathbf{z}'_{i+1}|\mu_0, t_{0,i+1})}{p(\mathbf{z}_i|\mu_0, t_{0,i+1})} \right\} \quad (7)$$

In each step, at most one kind of jump is applied to a sequence. Initially, define a probability  $Q < \frac{1}{2}$ , and the probability of birth, death and update as  $Q, Q, 1 - 2Q$ . In practice, we choose  $Q = \frac{1}{4}$ . However, there is a corner case: an empty PE sequence could not be applied with death or update. Therefore, for an empty sequence, only birth jump is in consideration, and the acceptance should be multiplied by  $Q$ . Accordingly, the acceptance of death jump on a single PE sequence should be divided by  $Q$ .

## 2.4 Extended RJMCMC for MCP-PMTs

In the dynode PMT, the single PE charge follows normal distribution. While in MCP-PMTs, the single MCPe charge follows normal distribution, and there is at least one MCPe for one PE. Therefore, MCPe should be changed during birth and death jumps, and  $\mathbf{z}$  should be redefined as the sequence of both the time of PEs and the corresponding MCPes:  $\mathbf{z} = \{(t_1, e_1), \dots, (t_N, e_N)\} \in (T, E)^N$ .

The birth jump is extended to 2 possible choices: to add a new PE, or add an MCPe for an existing PE. For one PE  $k$  with MCPe  $e_k$ , the possibility to increase MCPe should be

$$p(e'_k = e_k + 1|e_k) = \frac{G(e_k + 1)}{G(e_k)} \quad (8)$$

If no MCPe has been added, then a new PE is added with possibility should be

$$p(e'_{k+1} = 1|e_k) = 1 - \frac{1}{N_i} \sum_{e_k \in \mathbf{z}_i} \frac{G(e_k + 1)}{G(e_k)} \quad (9)$$

So, the acceptance of adding a new PE is:

$$\min \left\{ 1, \frac{p(\mathbf{z}'_{i+1}|\mu_0, t_{0,i+1})}{p(\mathbf{z}_i|\mu_0, t_{0,i+1})} \frac{\frac{1}{N'_{i+1}}}{h(t_+) \left(1 - \frac{1}{N_i} \sum_{e_k \in \mathbf{z}_i} \frac{G(e_k+1)}{G(e_k)}\right)} \right\} \quad (10)$$

With Eq. (A14), if no PE is to be added, the acceptance of adding an MCPe is:

$$\min \left\{ 1, \frac{p(\mathbf{w}|\mathbf{z}'_{i+1}, t_{0,i+1})}{p(\mathbf{w}|\mathbf{z}_i, t_{0,i+1})} \right\} \quad (11)$$

The death jump is changed to decrease an MCPe of an existing PE. If the original MCPe is 1, the PE will be removed. If there's one PE removed, the acceptance is

$$\min \left\{ 1, \frac{p(\mathbf{z}'_{i+1}|\mu_0, t_{0,i+1})}{p(\mathbf{z}_i|\mu_0, t_{0,i+1})} \frac{h(t_d) \left(1 - \frac{1}{N'_{i+1}} \sum_{e_k \in \mathbf{z}'_{i+1}} \frac{G(e_k+1)}{G(e_k)}\right)}{\frac{1}{N_i}} \right\} \quad (12)$$

while if only one MCPe is removed, the acceptance is the same as Eq. (11).

## 2.5 The prerequisites

The initial states of the Markov chain should be close to the truth, to make the chain converge faster. For example, when the truth light curve and  $t_0$  is known in Section 3, the initial value of  $t_0$  is the truth. Deconvolution is one good candidate. Consider the charge of PE to be a function of time  $q(t)$ , and ignore the white noise, the waveform is expressed as a convolution

$$\mathbf{w}(t) = \int q(\tau)V_{\text{PE}}(t - \tau)d\tau = q \otimes \tilde{V}_{\text{PE}} \quad (13)$$

Therefore, representing deconvolution with  $\oslash$ ,  $q$  is calculated by  $q = \mathbf{w} \oslash \tilde{V}_{\text{PE}}$ . Lucy [30] gives a deconvolution algorithm for the case that the elements of  $q$  are non-negative. Let  $r$  represent the step of iteration,

$$\begin{aligned} q^{r+1}(\tau) &= q^r(\tau) \sum_{t=\max\{\tau,0\}}^{\min\{l_w-1,\tau+l_V-1\}} \frac{\mathbf{w}(t)}{\mathbf{w}^r(t)} \tilde{V}_{\text{PE}}(t - \tau) \\ \mathbf{w}^r(t) &= \sum_{\tau=\max\{t,-l_V+1\}}^{\min\{l_w-1,t-l_V+1\}} q^r(\tau) \tilde{V}_{\text{PE}}(t - \tau) \end{aligned} \quad (14)$$

where  $t \in [0, l_w - 1]$ ,  $\tau \in [-l_V + 1, l_w - 1]$ .  $l_w$  represents the length of  $\mathbf{w}$ , and  $l_V$  represents the length of  $\tilde{V}_{\text{PE}}$ . The initial  $q^0$  could be any non-negative array that the summation is equal to the summation of  $\mathbf{w}$ . The two equations are two convolutions

$$\begin{aligned} q^{r+1}(\tau) &= q^r(\tau) \left( \frac{\mathbf{w}}{\mathbf{w}^r} \otimes \tilde{V}'_{\text{PE}} \right) (\tau + l_V - 1) \\ \mathbf{w}^r(t) &= (q^r \otimes \tilde{V}_{\text{PE}})(t) \end{aligned} \quad (15)$$

where  $\tilde{V}'_{\text{PE}}$  is the reverse array of  $\tilde{V}_{\text{PE}}$ .

In practice, we choose  $r$  up to 2000, and use the final  $q^{2000}(\tau)$  as the initial PE sequence. If all elements of  $q$  are smaller than 0.2, the corresponding waveform will be treated as a zero PE waveform, and will not be analyzed by FSMP. The times  $\tau$  where  $q^{2000}(\tau) > 0$  is the initial  $\mathbf{z}$ . As for the initial value of  $t_0$ , it depends on the light curve. When the light curve is unknown, the first PE time from the initial  $\mathbf{z}$  is used as  $t_0$ , and only  $\mathbf{z}$  is sampled in FSMP;  $q^{2000}(t)$  is also used as the temporary light curve  $\phi(t - t_0)$ , so the prior  $p(\mathbf{z}|\mu_0, t_0)$  and proposal  $h(t)$  in Section 2.3 are substituted correspondingly.

The solution space could be limited by the initial PE sequence provided by the deconvolution method. The limitation is optional, but decreases the execution time. Let the minimum and maximum PE time be  $t_{\min}$  and  $t_{\max}$ , the solution space *time window*  $\mathcal{T}$  is  $[t_{\min} - 4 \text{ ns}, t_{\max} + 4 \text{ ns}]$ . The definition range of  $\mathbf{w}$  should be also cut to  $[t_{\min} - 4 \text{ ns}, t_{\max} + 4 \text{ ns} + l_V]$ . 4 ns is an empirical value, to make the solution space

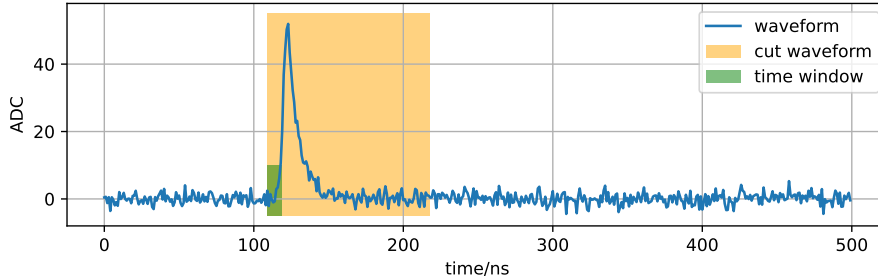


**Fig. 3:** The time window and solution space.

cover the truth. Fig. 3 shows the time window  $\mathcal{T}$  from the deconvolution result, and the cut waveform.

The probability of new PE time  $t_+$  in birth jump,  $h(t_+)$ , is the proposal distribution of  $t_+$  in RJMCMC. Although it could be any distribution covering the solution space, the chain will converge faster if it is proportional to the light curve  $\phi(t - t_0)$ . While  $\phi$  is already normalized to the whole time space, it should be normalized again to the solution space:

$$h(t) = \frac{\phi(t - t_0)}{\int_{\mathcal{T}} \phi(t - t_0) dt} \quad (16)$$

## 2.6 Towards energy reconstruction

The total energy of scintillator photons in the event is called visible energy. There are nonlinearities from event energy to visible energy [31]. The following discussion concentrates from waveform analysis, to the estimation and resolution of visible energy.

In Section 2.2,  $p(\mathbf{z}, t_0 | \mathbf{w})$  is calculated with a guessed  $\mu_0$ . To reconstruct the energy of the event, we still need an estimation of  $\mu$  with likelihood  $p(\mathbf{w} | \mu)$ ,

$$\hat{\mu}_{\text{MLE}} = \arg \max_{\mu} p(\mathbf{w} | \mu) \quad (17)$$

while

$$p(\mathbf{w} | \mu) = \sum_{\mathbf{z}, t_0} p(\mathbf{w} | \mathbf{z}, t_0) p(\mathbf{z}, t_0 | \mu) \quad (18)$$



Sample  $\mathbf{z}$  and  $t_0$  by FSMP in Section 2.3, with Eqs. (A1) and (3),

$$\begin{aligned}
p(\mathbf{w}|\mu) &= \sum_{\mathbf{z}, t_0} p(\mathbf{w}|\mathbf{z}, t_0) p(\mathbf{z}, t_0|\mu_0) \frac{p(\mathbf{z}, t_0|\mu)}{p(\mathbf{z}, t_0|\mu_0)} \\
&= p(\mathbf{w}|\mu_0) \sum_{\mathbf{z}, t_0} p(\mathbf{z}, t_0|\mathbf{w}) \frac{p(\mathbf{z}, t_0|\mu)}{p(\mathbf{z}, t_0|\mu_0)} \\
&= C \mathbb{E}_{\mathbf{z}, t_0} \left[ \frac{p(\mathbf{z}, t_0|\mu)}{p(\mathbf{z}, t_0|\mu_0)} \right] \\
&= \frac{C}{M} e^{-(\mu-\mu_0)} \sum_{\mathbf{z} \in \text{FSMP}} \left( \frac{\mu}{\mu_0} \right)^N
\end{aligned} \tag{19}$$

where  $C$  is a constant,  $M$  is the count of sampled  $\mathbf{z}$ , and  $N$  is the count of PE  $\mathbf{z}$ .  $\mathbb{E}_{\mathbf{z}, t_0}$  is expectation by  $\mathbf{z}, t_0$ , calculated by averaging over FSMP samples.

So the estimator  $\hat{\mu}_{\text{MLE}}$  should be the root of the equation

$$\frac{d}{d\mu} \log p(\mathbf{w}|\mu) = 0 \Leftrightarrow \sum_{\mathbf{z} \in \text{FSMP}} (\mu^N - N\mu^{N-1}) = 0 \tag{20}$$

### 3 Performance

To test the performance of FSMP, we simulate a neutrino detector with slow liquid scintillator [32] with 8-inch MCP-PMTs [11] that are the candidates of the Jinping Neutrino Experiment [6]. The normalized light curve  $\phi(t)$  in Fig. 4a and SER  $\tilde{V}_{\text{PE}}(t)$  in Fig. 4b are,

$$\begin{aligned}
\phi(t) &= \frac{\tau_1 + \tau_2}{\tau_2} \left( 1 - e^{-\frac{t}{\tau_1}} \right) e^{-\frac{t}{\tau_2}} \\
\tilde{V}_{\text{PE}}(t) &= \frac{1}{2\tau} e^{\frac{\sigma^2 - 2(t-4\sigma)\tau}{2\tau^2}} \left( 1 + \text{Erf} \left( -\frac{\sigma^2 - (t-4\sigma)\tau}{\sqrt{2}\sigma\tau} \right) \right)
\end{aligned} \tag{21}$$

where  $\tau_1 = 1.16$  ns,  $\tau_2 = 26.76$  ns,  $\sigma = 1.62$  ns,  $\tau = 7.2$  ns and Erf is the error function.

Table 1 shows the basic parameters. We first prepare sets of waveforms with fixed PE counts  $N$  from 0 to 125, sample  $N$  from a Poisson with parameter  $\mu$  and randomly choose a waveform from the corresponding set. The dataset for such a  $\mu$  consists of 10000 waveforms by repeating the procedures. To sample  $t_0$ , a uniform distribution between  $t_{0\text{min}}$  and  $t_{0\text{max}}$  is chosen:

$$p(t_0) = \frac{1}{t_{0\text{max}} - t_{0\text{min}}} \tag{22}$$

Two typical waveforms, one with  $\mu = 1, N = 2$  (waveform A) and one with  $\mu = 60, N = 96$  (waveform B), demonstrate the effectiveness of FSMP. To calculate convergence in Section 3.2, initial PE sequence is randomly chosen in the time window  $\mathcal{T}$  provided in Section 2.5. The initial PE count ranges from 0 to 31 and 86 to 106 for

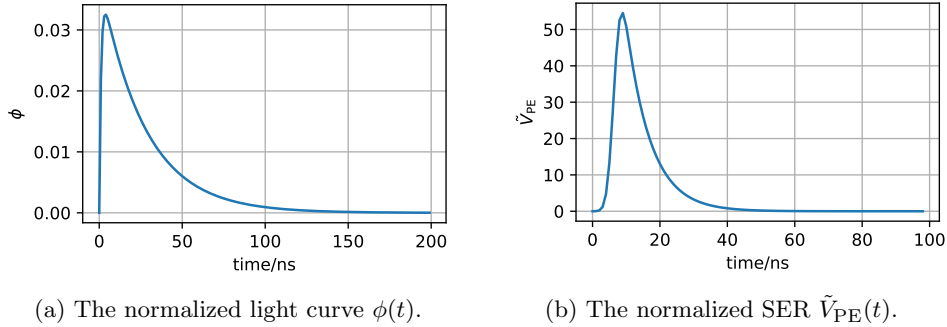


**Fig. 4:** Figures of light curve and SER in simulation.

**Table 1:** The basic parameters used in the simulation.

Parameter	Value
$\mu$	0.1, 0.2, 0.5, 1, 2, ..., 10, 15, ..., 60
$t_{0\min}$	100 ns
$t_{0\max}$	200 ns
Baseline $\sigma_\epsilon$	1.59(ADC)
Single MCPe charge $q$	597.88(ADC·ns)
Single MCPe charge $\sigma_q$	201.28(ADC·ns)
Waveform length	500 ns
Sampling rate	1/ns
Waveform samples per $\mu$	10000
MCPe 1st peak $G(1)$	64.6 %
MCPe 2nd peak $G(2)$	23.2 %
MCPe 3rd peak $G(3)$	7.64 %
MCPe 4th peak $G(4)$	4.53 %

waveforms A and B. The initial and last sampled sequence is shown in Fig. 5. No matter what the initial sequence is, FSMP samples the correct parameters reproducing the input waveform.

### 3.1 Execution Speed and Precision

FSMP makes extensive use of linear algebraic procedures as shown in Section A.1. Fig. 6 shows our *batched* strategy [33] to accelerate FSMP, stacking the quantities of scalars, vectors and matrices from different waveforms into tensors with one extra batched dimension. The PE sequence,  $\mathbf{z} = (t_1, t_2, \dots)$  is a vector with various lengths. We pad the short sequence with zeros to form the batched matrix, and introduce a new vector to store the number of PEs  $N$  of each waveform. Batching allows FSMP to be implemented in NumPy [34] and CuPy [35] efficiently for CPU and GPU executions.

Fig. 7a shows the comparison of performance on CPU and GPU. With small batch sizes, running all computation on CPU is faster than offloading to GPU, because data transfer between GPU and GPU takes time. When the batch size increases, GPU gains

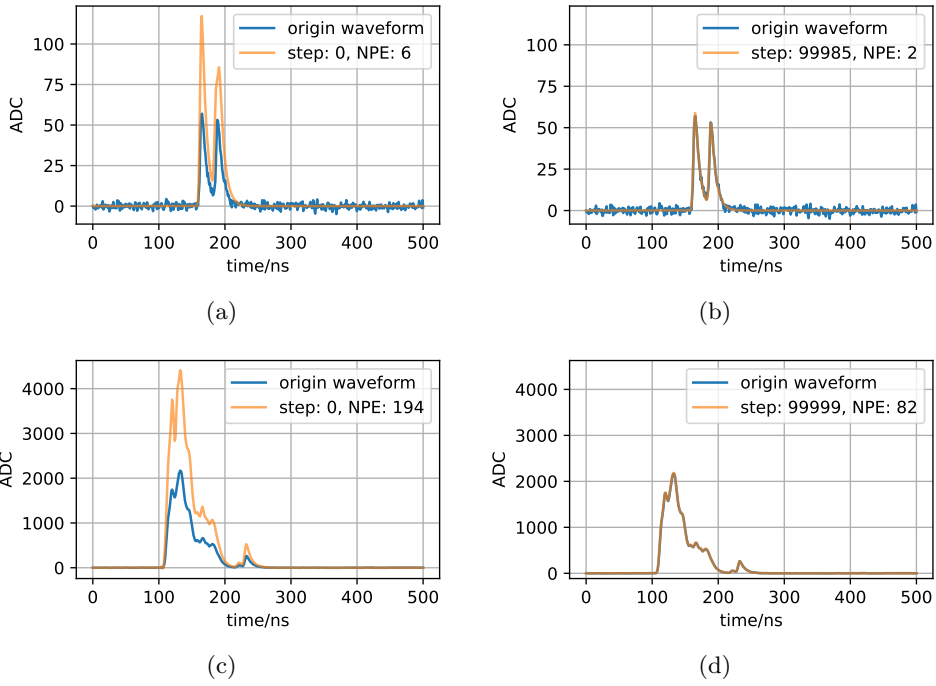
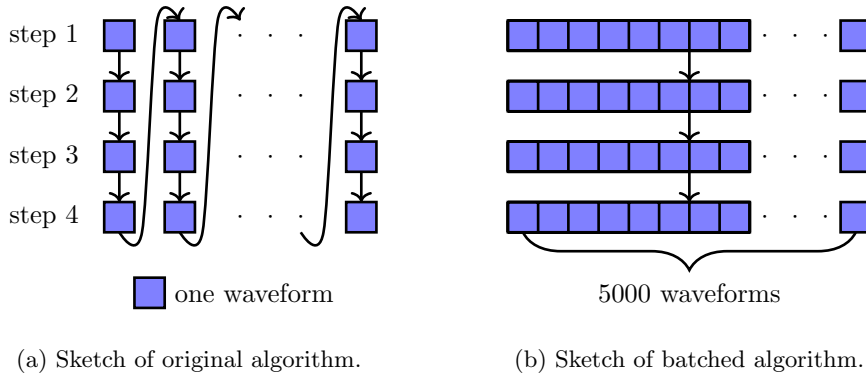


**Fig. 5:** Example of two Markov chains, upper figures for waveform A and lower for B, initial sample on the left and the last sample on the right. Orange lines are the predicted waveforms, getting closer to the original ones with the chain.



(a) Sketch of original algorithm.

(b) Sketch of batched algorithm.

**Fig. 6:** A comparison of original algorithm and batched one. One square represents the data related to one waveform, and the arrows shows the execution directions.

performance on matrix computations up to 100 waveforms per second. The execution speed of CPU is mostly independent of batch size.

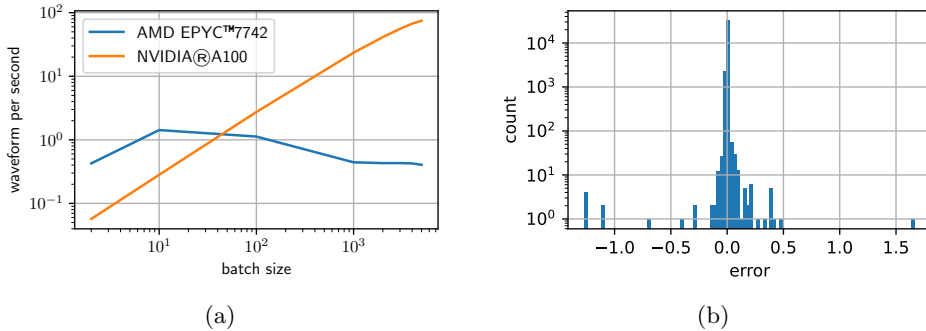


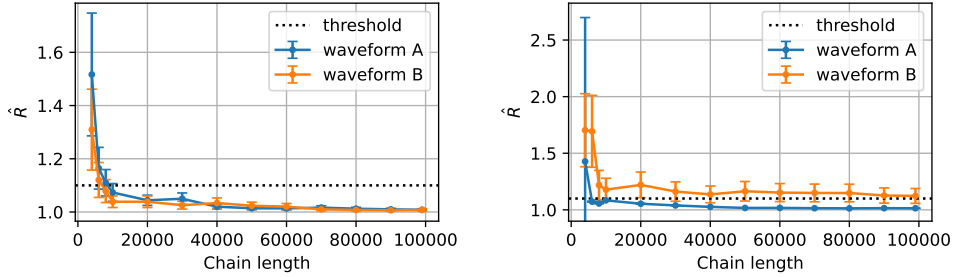
**Fig. 7:** FSMP comparison with (a) execution speed and (b) error of  $\Delta\nu$ , the waveform log-likelihood ratio of two PE sequences in Eq. (A11), on a single core of AMD EPYC™7742 CPU and NVIDIA®A100 GPU.

Matrix calculation may induce float-point rounding errors. We use `float64` on CPU because its native instruction set is 64-bit. To better utilize the computation units [36], we choose `float32` on GPU but with a risk of lower precision. For comparison, every accepted step in the RJMCMC chain is recorded. After the GPU version program, the waveform log-likelihood ratio of two PE sequences  $\Delta\nu$  in Eq. (A11) is calculated by the CPU again. Fig. 7b shows the error of  $\Delta\nu$  of each step for waveform B, with deconvolution provided initial PE sequence. The absolute value of error is mainly within 1.0.

### 3.2 Convergence

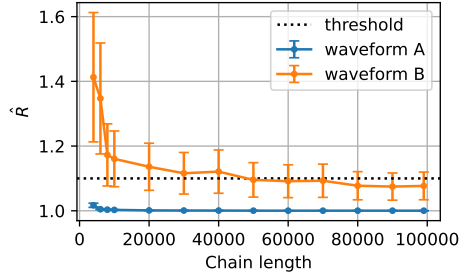
The Gelman-Rubin diagnostic checks whether a Metropolis-Hastings Markov chain is convergent [37]. It calculates a convergence indicator  $\hat{R}$  from multiple auxiliary chains with different initial conditions as a combination of within-group deviation and between-group deviation, which shows the consistency within each chain and among all chains. The chain is regarded as convergent when  $\hat{R} < 1.1$ . We chose the sampled time offset  $t_0$  and the number of PEs  $N$ . Figs. 8a and 8b show the convergence of  $t_0$  and  $N$  of the two waveforms in Fig. 5. The slower convergence of waveform B is expected for so large the solution space that the initial conditions of the chains are diverse.

PE sequence  $\mathbf{z}$ , although being the most important results from FSMP, is not suitable to directly compute  $\hat{R}$  which requires a fixed-dimensional input. Brooks and Galman [38] suggested several distance measures to quantify the similarity between trans-dimensional samples. Wasserstein distance [39] is such a distance measurement, and is chosen as a requirement of the convergence of PE sequence. Define MCPe sequence as all times of MCPes, and calculate the Wasserstein distance between MCPe sequence and an empty sequence as the scalar to use in calculating Gelman-Rubin



(a)  $t_0$  convergence of two waveforms.

(b)  $N$  convergence of two waveforms.



(c)  $z$  convergence of two waveforms.

**Fig. 8:** The convergence of different representative scalars. The error bar represents the upper confidence limits of  $\hat{R}$ .

diagnostic. As Wasserstein distance could not handle empty sequences, a dummy PE at  $t = 0$  is added to all PE sequences, with a very small weight  $10^{-9}$ . Fig. 8c shows the convergence of MCPe sequence of the two waveforms discussed above. The basic trending is similar to the convergence of  $t_0$  and  $N$ .

### 3.3 Bias and resolution

The estimator  $\hat{t}_0$  should be the average value of the sampled  $t_0$  chain. For comparison, we also sampled a chain of  $t_0$  from true PE sequence, labeled “MCMC” in the figures. Another comparison is to use the first peak 10% rise time [11] as the biased estimator of  $t_0$ . The resolution is defined by

$$\eta_t = \frac{\sqrt{\text{Var}[\hat{t}_0]}}{\text{E}[\hat{t}_0]} \quad (23)$$

Fig. 9a shows the bias of  $\hat{t}_0$ , and Fig. 9b shows the resolution. The result shows that the bias is around 0.1 ns, and when  $\mu < 20$ , FSMP gives better time resolution than first PE time.

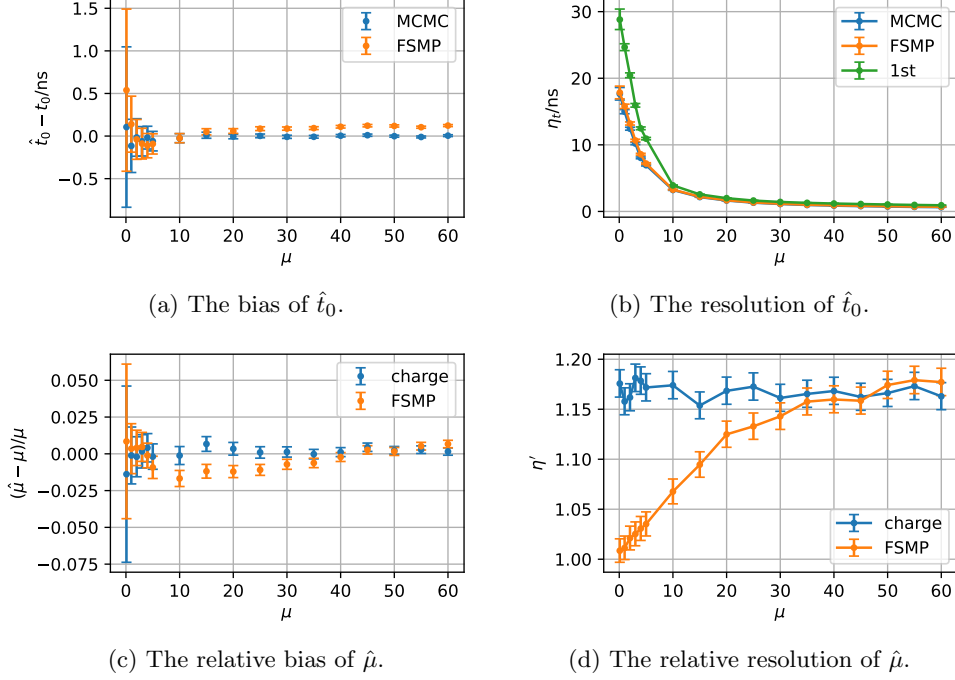


**Fig. 9:** The bias and resolution of  $\hat{t}_0$  and  $\hat{\mu}$  from FSMP, compared with other methods. 90% confidence interval.

The energy resolution of  $\hat{\mu}$  is compared with the charge method. Define the charge of a waveform as  $Q$ , and estimation of  $\mu$  as below, and  $\hat{\mu}_{\text{charge}}$  is proved to be unbiased:

$$\hat{\mu}_{\text{charge}} = \frac{Q}{q_e}, q_e = \sum_{e=1}^4 G(e)eq \quad (24)$$

$$\text{E}[Q] = \text{E}[N]q_e = \mu q_e \Rightarrow \text{E}[\hat{\mu}_{\text{charge}}] = \mu \quad (25)$$

The relative bias of  $\hat{\mu}$  is defined as the bias divided by the truth value  $(\hat{\mu} - \mu)/\mu$ . The resolution  $\eta$  [40] and relative resolution  $\eta'$  of  $\hat{\mu}$  is defined as

$$\eta = \frac{\sqrt{\text{Var}[\hat{\mu}]}}{\text{E}[\hat{\mu}]}, \eta' = \frac{\eta}{\eta_{\text{theory}}} \quad (26)$$

where  $\eta_{\text{theory}}$  is the theoretical energy resolution. For both MLE in Section 2.6 and charge method, the theoretical resolution is the resolution of  $N$ , which is an unbiased MLE estimator of  $\mu$ .

$$\eta_{\text{theory}} = \frac{\sqrt{\text{Var}[N]}}{\text{E}[N]} \quad (27)$$

Any waveform analysis result shouldn't give better  $\mu$  estimation than using the PE truth. Therefore,  $\eta'$  should be always larger than 1.

FSMP in Section 2.2 requires  $\mu_0$  value in the prior  $p(\mathbf{z}|\mu_0)$ . Here it is sampled from a gamma distribution  $\Gamma(\alpha = 2\mu, \beta = 2)$  for each waveform. The expectation of this sampling is the truth value  $\mu$ , while the variance is  $\frac{\mu}{2}$ . It imitates the reality, when we don't exactly know the real  $\mu$ .

Figs. 9c and 9d show the comparison result. When  $\mu$  is relatively small, the resolution of FSMP method is better than charge method. Here is a qualitative explanation: when  $\mu$  is small, number of PEs is also small. FSMP method should give more precise result in that case, because the possibility pile-up is rare. When  $\mu$  is large,  $\hat{\mu}$  from FSMP is still more biased than charge method. Charge method should be used in that case, because FSMP cannot give a better resolution. Choosing  $\mu = 1$  as the standard, FSMP is  $(12.5 \pm 1.4)\%$  better than charge method in estimation of  $\mu$ . This conclusion could lead to the resolution of visible energy that, in the most optimistic case, FSMP improves the resolution of visible energy by 12%.

## 4 Analyze real data

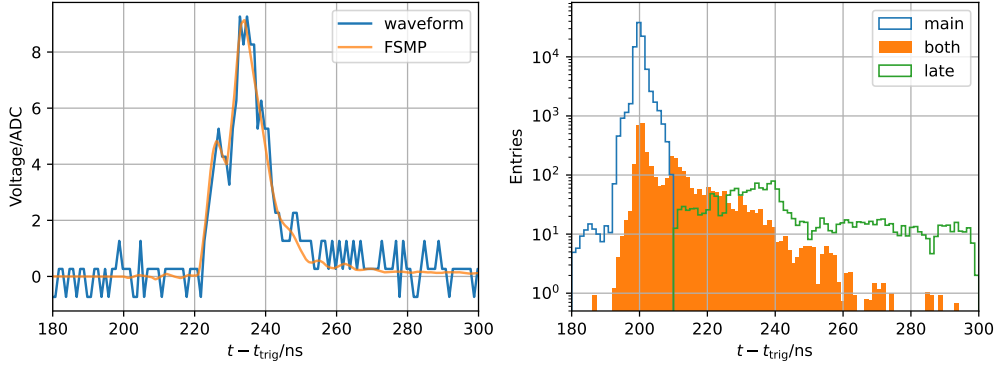
Zhang et al. [11] studied the performance of a new type 8-inch MCP-PMT. This section re-analyze the experimental data from their work to show the advantage of FSMP. The light curve and  $\mu_0$  is substituted following Section 2.5, and SER is obtained from Zhang's method. Only PE times are sampled with RJMCMC, and  $t_0$  is not sampled because the light curve is not available, according to Section 2.5.

Fig. 10a shows a sample waveform. The FSMP sampled PE sequences are convoluted with single PE response, restored and averaged to the orange waveform. FSMP fits all peaks of the waveform well. Fig. 10b shows all PE samples of a PMT in a single run. The blue and green histogram represent the sampled PEs only before and only after 210 ns in each waveform samples. The orange filled histogram are the remaining samples. The orange one contains true-secondary electrons, while the green one is *late pulse*, which may contain the back-scattered and rediffused electrons. The figures demonstrate that FSMP gives all PE times from waveforms, and provides possibility to analyze the orange histogram and dig through the physical process with quantitative method.

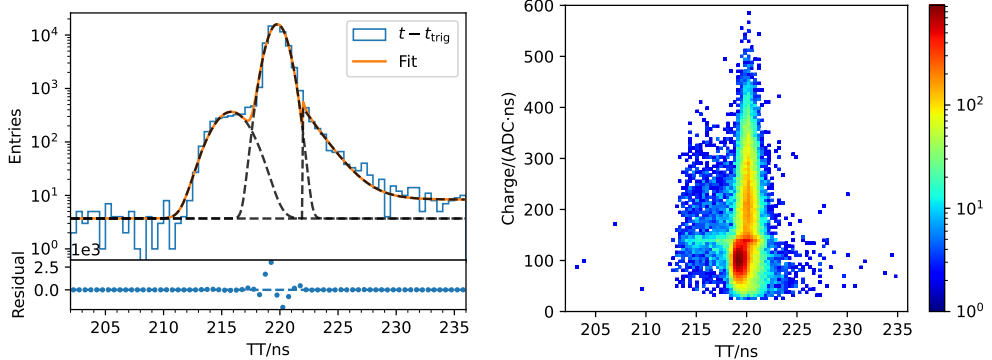
To compare the transition time spread (TTS) with Zhang's method, the transition time (TT) is defined as the interval between trigger time and the average first PE time of the samples of each waveform. Fig. 10d shows the histogram of charge and TT in logarithmic scale. The distribution of TT is fit in Fig. 10c. The fit TTS is  $(1.703 \pm 0.007)$  ns, better than the result  $(1.719 \pm 0.001)$  ns with Zhang's method.

## 5 Conclusion

We gave an introduction of FSMP method. It is a flexible and general Bayesian-based RJMCMC to sample PE sequence from posterior distribution. It is applied on both dynode PMT and ALD-coated MCP-PMT with jumbo charge outputs. FSMP makes full use of pulse shape and amplitude information to estimate the full PE sequence,



(a) Average restored waveform of all sampled PE sequences of one waveform. (b) The PE times sampled by FSMP, showing the main pulse and the late pulse.



(c) Fit of TT spread (TTS). (d) The 2D distribution of charge and TT.

**Fig. 10:** Analysis of MCP-PMT testing data.

which gives better precision. The GPU acceleration makes FSMP fast enough for large amount of waveform in experiments.

Applying FSMP to our simulated waveforms, it gives  $(12.5 \pm 1.4)\%$  better resolution of  $\hat{\mu}$  when  $\mu = 1$ . When  $\mu < 20$ , it performs better than charge method in estimating  $\mu$  and better than 1st PE time in estimating  $t_0$ . Therefore, for MeV neutrino experiments in liquid scintillator detectors, *e.g.*, Jinping Neutrino Experiment and JUNO, FSMP could improve resolution of visible energy by 12% in optimistic case.

## 6 Acknowledgements

We would like to acknowledge the valuable contributions of Shengqi Chen. He gave us much help on porting the algorithm to GPU, and much assistance on profiling. His professionalism on high performance computing is highly appreciated. We are also grateful to Zhuojing Zhang for her inspirational guidance to RJMCMC and Prof. Zhirui Hu



for the discussions on the convergence of Markov Chain Monte Carlo. Much appreciation to Tsinghua University TUNA Association, for the opportunity to communicate about our ideas on GPU programming.

Many thanks to Jun Weng for his patient guidance on MCP-PMT. He was one of the first FSMP users, and gave us a lot of helpful advice. Chuang Xu and Yiqi Liu deserve our appreciation on trying FSMP with experimental data. We are also thankful to Wentai Luo and Ye Liang for their expertise on the time properties of liquid scintillator. Thanks to other colleagues in Center for High Energy Physics for their assistance. Their help is necessary and indispensable.

This work was supported by the National key research and development program of China (Grant no. 2023YFA1606104, 2022YFA1604704), in part by the National Natural Science Foundation of China (No. 12127808) and the Key Laboratory of Particle and Radiation Imaging (Tsinghua University). Part of the GPU computing was supported by the Center of High Performance Computing, Tsinghua University.

## Appendix A Calculation of possibilities

### A.1 For FSMP

First we need to calculate  $p(\mathbf{z}|\mu, t_0)$  for Eq. (3). This possibility depends on the light curve. It is calculated as

$$\begin{aligned} p(\mathbf{z}|\mu, t_0)d\mathbf{z} &= e^{-\mu} \prod_{k=1}^N \mu \phi(t_k - t_0) dt_k \\ &= e^{-\mu} \mu^N \prod_{k=1}^N \phi(t_k - t_0) dt_k \\ &= e^{-\mu} \mu^N \phi(\mathbf{z} - t_0) d\mathbf{z} \end{aligned} \tag{A1}$$

while  $\phi(\mathbf{z} - t_0)d\mathbf{z}$  is an abbreviation of  $\prod_{k=1}^N \phi(t_k - t_0) dt_k$ .

Then we need to calculate  $p(\mathbf{w}|\mathbf{z})$ . Assume it is a multivariate normal distribution, and  $\tilde{V}_{\text{PE}}(t)$  is the normalized single PE response (SER) of a PMT (see Section 2.1), and the variance of white noise is  $\sigma_\epsilon^2$ . Each value of the waveform  $\mathbf{w}(t_w)$  follows Normal distribution  $\mathcal{N}(\mathbf{U}(\mathbf{z}), \mathbf{\Sigma}(\mathbf{z}))$ , where

$$\begin{aligned} U_w &:= \sum_{k=1}^N q_k \tilde{V}_{\text{PE}}(t_w - t_k) \\ \Sigma_{wv} &:= \sum_{k=1}^N \sigma_q^2 \tilde{V}_{\text{PE}}(t_w - t_k) \tilde{V}_{\text{PE}}(t_v - t_k) + \sigma_\epsilon^2 \delta_{wv} \\ &= \sum_{k=1}^N \Xi(t_w - t_k, t_v - t_k) + \sigma_\epsilon^2 \delta_{wv} \end{aligned} \tag{A2}$$

Tipping [41, 42] proved that in this model, we can write down

$$\log p(\mathbf{w}|\mathbf{z}) = -\frac{N_w}{2} \log(2\pi) - \frac{1}{2} \log |\boldsymbol{\Sigma}| - \frac{1}{2} (\mathbf{w} - \mathbf{U})^\top \boldsymbol{\Sigma}^{-1} (\mathbf{w} - \mathbf{U}) \quad (\text{A3})$$

where  $N_w$  is the length of the waveform, and  $\Xi$  is represented by direct product

$$\Xi = \mathbf{a}_0 \Lambda_0 \mathbf{a}_0^\top, \quad a_{0,wv} = \tilde{V}_{\text{PE}}(t_w - t_v), \quad \Lambda_{0,wv} = \sigma_q^2 \delta_{wv} \quad (\text{A4})$$

The update jump is a combination of death jump at  $t_-$  and birth jump at  $t_+ = t_- + \Delta t$ . We can combine the two jumps into one operation. For  $\mathbf{z}'_{i+1}, t_-, t_+$  in Fig. 2c, define the waveform of PE  $t_-$  as  $\mathbf{a}_{w-} = V_{\text{PE}}(t_w - t_-)$ , aka  $\mathbf{a}_-$ . Simultaneously, define  $\mathbf{a}_+$  as the single PE waveform of  $t_+$ . Combine the two waveform into a matrix  $\mathbf{a} = (\mathbf{a}_-, \mathbf{a}_+)$ , we get

$$\begin{aligned} \Delta \boldsymbol{\Sigma} &= \Xi(\mathbf{z}') - \Xi(\mathbf{z}) = \mathbf{a} \Lambda \mathbf{a}^\top \\ \Lambda &:= \sigma_q^2 \begin{bmatrix} -1 & \\ & 1 \end{bmatrix}. \end{aligned} \quad (\text{A5})$$

For a birth jump, we can define  $\mathbf{a}_- = 0$ ; for a death jump, define  $\mathbf{a}_+ = 0$ . Then we can unify the 3 kinds of jump into one formula.

RJMCMC only requires the ratio of  $p(\mathbf{w}|\mathbf{z})$ , thus we only need to calculate

$$\begin{aligned} \log \frac{p(\mathbf{w}|\mathbf{z}')}{p(\mathbf{w}|\mathbf{z})} &= -\frac{1}{2} (\Delta T + \Delta R) \\ \Delta T &:= \log \left( \frac{|\boldsymbol{\Sigma}(\mathbf{z}')|}{|\boldsymbol{\Sigma}(\mathbf{z})|} \right) \\ \Delta R &:= [\mathbf{w} - \mathbf{U}(\mathbf{z}')]^\top \boldsymbol{\Sigma}^{-1}(\mathbf{z}') [\mathbf{w} - \mathbf{U}(\mathbf{z}')] - [\mathbf{w} - \mathbf{U}(\mathbf{z})]^\top \boldsymbol{\Sigma}^{-1}(\mathbf{z}) [\mathbf{w} - \mathbf{U}(\mathbf{z})] \\ &= (\mathbf{y} - \Delta \mathbf{U})^\top \boldsymbol{\Sigma}^{-1}(\mathbf{z}') (\mathbf{y} - \Delta \mathbf{U}) - \mathbf{y}^\top \boldsymbol{\Sigma}^{-1}(\mathbf{z}) \mathbf{y}. \end{aligned} \quad (\text{A6})$$

where  $\mathbf{y} := \mathbf{w} - \mathbf{U}(\mathbf{z})$ . Like Eq. (A5),

$$\begin{aligned} \Delta \mathbf{U} &:= \mathbf{U}(\mathbf{z}') - \mathbf{U}(\mathbf{z}) \\ &= q(-\mathbf{a}_- + \mathbf{a}_+) \\ &= \mathbf{a} \boldsymbol{\lambda} \\ \boldsymbol{\lambda} &:= q \begin{bmatrix} -1 \\ 1 \end{bmatrix}. \end{aligned} \quad (\text{A7})$$

Therefore, the most important item is  $\boldsymbol{\Sigma}^{-1}$ . Let  $\mathbf{c} := \boldsymbol{\Sigma}^{-1} \mathbf{a}$ ,  $\mathbf{B} := (\Lambda^{-1} + \mathbf{a}^\top \mathbf{c})^{-1}$ , we have Woodbury formula [43]

$$\begin{aligned} \boldsymbol{\Sigma}^{-1}(\mathbf{z}') &= (\boldsymbol{\Sigma} + \mathbf{a} \Lambda \mathbf{a}^\top)^{-1} \\ &= \boldsymbol{\Sigma}^{-1} - \boldsymbol{\Sigma}^{-1} \mathbf{a} (\Lambda^{-1} + \mathbf{a}^\top \boldsymbol{\Sigma}^{-1} \mathbf{a})^{-1} \mathbf{a}^\top \boldsymbol{\Sigma}^{-1} \\ &= \boldsymbol{\Sigma}^{-1} - \mathbf{c} \mathbf{B} \mathbf{c}^\top. \end{aligned} \quad (\text{A8})$$

Calculate  $\Delta R$  with Eqs. (A6) to (A8):

$$\begin{aligned}\Delta R &= (\mathbf{y} - \mathbf{a}\boldsymbol{\lambda})^\top (\boldsymbol{\Sigma}^{-1} - \mathbf{c}\mathbf{B}\mathbf{c}^\top) (\mathbf{y} - \mathbf{a}\boldsymbol{\lambda}) - \mathbf{y}^\top \boldsymbol{\Sigma}^{-1} \mathbf{y} \\ &= -\Upsilon^\top \mathbf{B}\Upsilon + \boldsymbol{\lambda}^\top \boldsymbol{\Lambda}^{-1} \boldsymbol{\lambda}\end{aligned}\quad (\text{A9})$$

where  $\Upsilon := \mathbf{c}^\top \mathbf{y} + \boldsymbol{\Lambda}^{-1} \boldsymbol{\lambda}$ .

Calculate  $\Delta T$  with Eqs. (A5) and (A8):

$$\begin{aligned}\Delta T &= \log \left( \frac{|\boldsymbol{\Sigma} + \mathbf{a}\boldsymbol{\Lambda}\mathbf{a}^\top|}{|\boldsymbol{\Sigma}|} \right) \\ &= \log (|1 + \mathbf{a}\boldsymbol{\Lambda}\mathbf{a}^\top \boldsymbol{\Sigma}^{-1}|) \\ &= \log (|\boldsymbol{\Lambda}\mathbf{B}^{-1}|) \\ &= -\log (|\mathbf{B}\boldsymbol{\Lambda}^{-1}|)\end{aligned}\quad (\text{A10})$$

With Eqs. (A6), (A9) and (A10), define  $\Delta\nu$ :

$$\Delta\nu = \log \frac{p(\mathbf{w}|\mathbf{z}')}{p(\mathbf{w}|\mathbf{z})} = \frac{1}{2} (\Upsilon^\top \mathbf{B}\Upsilon - \boldsymbol{\lambda}^\top \boldsymbol{\Lambda}^{-1} \boldsymbol{\lambda} + \log (|\mathbf{B}\boldsymbol{\Lambda}^{-1}|)) \quad (\text{A11})$$

From Eqs. (A1) and (A11), we have

$$\frac{p(\mathbf{z}'|\mu_0, t_0)}{p(\mathbf{z}|\mu_0, t_0)} = \frac{p(\mathbf{w}|\mathbf{z}')p(\mathbf{z}'|\mu_0, t_0)}{p(\mathbf{w}|\mathbf{z})p(\mathbf{z}|\mu_0, t_0)} = e^{\Delta\nu} \mu_0^{N'-N} \frac{\phi(\mathbf{z}' - t_0)}{\phi(\mathbf{z} - t_0)} \quad (\text{A12})$$

## A.2 For extended FSMP

Obviously we have

$$\sum_{e \in E} G(e) = 1 \quad (\text{A13})$$

which means that  $G$  is a PDF of a discrete distribution. Then we can recalculate probability

$$p(\mathbf{z}|\mu) d\mathbf{z} = e^{-\mu} \mu^N \prod_{k=1}^N \phi(t_k - t_0) G(e_k) dt_k \quad (\text{A14})$$

Considering  $e_k$ , we should redefine

$$\begin{aligned}U_w &:= \sum_{k=1}^N e_k q_k \tilde{V}_{\text{PE}}(t_w - t_k) \\ \Sigma_{wv} &:= \sum_{k=1}^N e_k \Xi_{\text{PE}}(t_w - t_k, t_v - t_k) + \sigma_\epsilon^2 \delta_{wv} \\ \boldsymbol{\Lambda} &:= \sigma_q^2 \begin{bmatrix} -e_- & \\ & e_+ \end{bmatrix}\end{aligned}\quad (\text{A15})$$

For update jump,  $e_- = e_+ = e_k$ ; for others,  $e_- = e_+ = 1$ . With the same derivation in Section A.1, we can calculate  $\Delta\nu$ , and finally  $\frac{p(\mathbf{z}'_{i+1})}{p(\mathbf{z}_i)}$ .

## References

- [1] KamLAND Collaboration, Gando, A., Gando, Y., Hanakago, H., Ikeda, H., Inoue, K., Ishidoshiro, K., Ishikawa, H., Koga, M., Matsuda, R., Matsuda, S., Mitsui, T., Motoki, D., Nakamura, K., Obata, A., Oki, A., Oki, Y., Otani, M., Shimizu, I., Shirai, J., Suzuki, A., Takemoto, Y., Tamae, K., Ueshima, K., Watanabe, H., Xu, B.D., Yamada, S., Yamauchi, Y., Yoshida, H., Kozlov, A., Yoshida, S., Piepke, A., Banks, T.I., Fujikawa, B.K., Han, K., O'Donnell, T., Berger, B.E., Learned, J.G., Matsuno, S., Sakai, M., Efremenko, Y., Karwowski, H.J., Markoff, D.M., Tornow, W., Detwiler, J.A., Enomoto, S., Decowski, M.P.: Reactor on-off antineutrino measurement with KamLAND. *Physical Review D* **88**(3), 033001 (2013) <https://doi.org/10.1103/PhysRevD.88.033001> . Publisher: American Physical Society. Accessed 2023-10-28
- [2] Gatti, F., Lagomarsino, V., Musico, P., Pallavicini, M., Razeto, A., Testera, G., Vitale, S.: The Borexino read out electronics and trigger system. *Nuclear Instruments and Methods in Physics Research Section A: Accelerators, Spectrometers, Detectors and Associated Equipment* **461**(1), 474–477 (2001) [https://doi.org/10.1016/S0168-9002\(00\)01275-4](https://doi.org/10.1016/S0168-9002(00)01275-4) . Number: 1. Accessed 2020-10-09
- [3] Anfimov, N.: Large photocathode 20-inch PMT testing methods for the JUNO experiment. *Journal of Instrumentation* **12**(06), 06017 (2017) <https://doi.org/10.1088/1748-0221/12/06/C06017> . Accessed 2023-03-04
- [4] Beacom, J.F., Chen, S., Cheng, J., Doustimotlagh, S.N., Gao, Y., Gong, G., Gong, H., Guo, L., Han, R., He, H.-J., Huang, X., Li, J., Li, J., Li, M., Li, X., Liao, W., Lin, G.-L., Liu, Z., McDonough, W., Šrámek, O., Tang, J., Wan, L., Wang, Y., Wang, Z., Wang, Z., Wei, H., Xi, Y., Xu, Y., Xu, X.-J., Yang, Z., Yao, C., Yeh, M., Yue, Q., Zhang, L., Zhang, Y., Zhao, Z., Zheng, Y., Zhou, X., Zhu, X., Zuber, K.: Physics prospects of the Jinping neutrino experiment. *Chinese Physics C* **41**(2), 023002 (2017) <https://doi.org/10.1088/1674-1137/41/2/023002> . Publisher: IOP Publishing. Accessed 2022-05-09
- [5] Xu, B.: Jinping Neutrino Experiment: a Status Report. *Journal of Physics: Conference Series* **1468**(1), 012212 (2020) <https://doi.org/10.1088/1742-6596/1468/1/012212> . Publisher: IOP Publishing. Accessed 2022-11-20
- [6] Xu, B.: Design and Construction of hundred-ton liquid neutrino detector at CJPL II. *PoS ICHEP2022*, 926 (2022) <https://doi.org/10.22323/1.414.0926>
- [7] Abe, K., Hiraide, K., Ichimura, K., Kishimoto, Y., Kobayashi, K., Kobayashi, M., Moriyama, S., Nakahata, M., Ogawa, H., Sato, K., Sekiya, H., Suzuki, T., Takachio, O., Takeda, A., Tasaka, S., Yamashita, M., Yang, B.S., Kim, N.Y., Kim, Y.D., Itow, Y., Kanzawa, K., Masuda, K., Martens, K., Suzuki, Y., Xu, B.D., Miuchi, K., Oka, N., Takeuchi, Y., Kim, Y.H., Lee, K.B., Lee, M.K., Fukuda, Y., Miyasaka, M., Nishijima, K., Fushimi, K., Kanzaki, G., Nakamura, S.: A measurement of the scintillation decay time constant of nuclear recoils in liquid

xenon with the XMASS-I detector. *Journal of Instrumentation* **13**(12), 12032–12032 (2018) <https://doi.org/10.1088/1748-0221/13/12/P12032> . Publisher: IOP Publishing. Accessed 2022-07-26

- [8] Readout electronics and data acquisition system of PandaX-4T experiment - IOPscience. <https://iopscience.iop.org/article/10.1088/1748-0221/17/02/T02004> Accessed 2024-03-05
- [9] Collaboration, T.L., Akerib, D.S., Akerlof, C.W., Akimov, D.Y., Alsum, S.K., Araújo, H.M., Bai, X., Bailey, A.J., Balajthy, J., Balashov, S., Barry, M.J., Bauer, P., Beltrame, P., Bernard, E.P., Bernstein, A., Biesiadzinski, T.P., Boast, K.E., Bolozdynya, A.I., Boulton, E.M., Bramante, R., Buckley, J.H., Bugaev, V.V., Bunker, R., Burdin, S., Busenitz, J.K., Carels, C., Carlsmith, D.L., Carlson, B., Carmona-Benitez, M.C., Cascella, M., Chan, C., Cherwinka, J.J., Chiller, A.A., Chiller, C., Craddock, W.W., Currie, A., Cutter, J.E., Cunha, J.P., Dahl, C.E., Dasu, S., Davison, T.J.R., Viveiros, L., Dobi, A., Dobson, J.E.Y., Druzzkiewicz, E., Edberg, T.K., Edwards, B.N., Edwards, W.R., Elnimr, M.M., Emmet, W.T., Faham, C.H., Fiorucci, S., Ford, P., Francis, V.B., Fu, C., Gaitskell, R.J., Gantos, N.J., Gehman, V.M., Gerhard, R.M., Ghag, C., Gilchriese, M.G.D., Gomber, B., Hall, C.R., Harris, A., Haselschwardt, S.J., Hertel, S.A., Hoff, M.D., Holbrook, B., Holtom, E., Huang, D.Q., Hurteau, T.W., Ignarra, C.M., Jacobsen, R.G., Ji, W., Ji, X., Johnson, M., Ju, Y., Kamdin, K., Kazkaz, K., Khaitan, D., Khazov, A., Khromov, A.V., Konovalov, A.M., Korolkova, E.V., Kraus, H., Krebs, H.J., Kudryavtsev, V.A., Kumpan, A.V., Kyre, S., Larsen, N.A., Lee, C., Lenardo, B.G., Lesko, K.T., Liao, F.-T., Lin, J., Lindote, A., Lippincott, W.H., Liu, J., Liu, X., Lopes, M.I., Lorenzon, W., Luitz, S., Majewski, P., Malling, D.C., Manalaysay, A.G., Manenti, L., Mannino, R.L., Markley, D.J., Martin, T.J., Marzoni, M.F., McKinsey, D.N., Mei, D.-M., Meng, Y., Miller, E.H., Mock, J., Monzani, M.E., Morad, J.A., Murphy, A.S.J., Nelson, H.N., Neves, F., Nikkel, J.A., O'Neill, F.G., O'Dell, J., O'Sullivan, K., Olevitch, M.A., Oliver-Mallory, K.C., Palladino, K.J., Pangilinan, M., Patton, S.J., Pease, E.K., Piepke, A., Powell, S., Preece, R.M., Pushkin, K., Ratcliff, B.N., Reichenbacher, J., Reichhart, L., Rhyne, C., Rodrigues, J.P., Rose, H.J., Rosero, R., Saba, J.S., Sarychev, M., Schnee, R.W., Schubnell, M.S.G., Scovell, P.R., Shaw, S., Shutt, T.A., Silva, C., Skarpaas, K., Skulski, W., Solovov, V.N., Sorensen, P., Sosnovtsev, V.V., Stancu, I., Stark, M.R., Stephenson, S., Stiegler, T.M., Sumner, T.J., Sundarnath, K., Szydagis, M., Taylor, D.J., Taylor, W., Tennyson, B.P., Terman, P.A., Thomas, K.J., Thomson, J.A., Tiedt, D.R., To, W.H., Tomás, A., Tripathi, M., Tull, C.E., Tvrznikova, L., Uvarov, S., Va'vra, J., Grinten, M.G.D., Verbus, J.R., Vuosalo, C.O., Waldron, W.L., Wang, L., Webb, R.C., Wei, W.-Z., While, M., White, D.T., Whitis, T.J., Wisniewski, W.J., Witherell, M.S., Wolfs, F.L.H., Woods, E., Woodward, D., Worm, S.D., Yeh, M., Yin, J., Young, S.K., Zhang, C.: LUX-ZEPLIN (LZ) Conceptual Design Report (2015)
- [10] Zhang, H.Q., Wang, Z.M., Zhang, Y.P., Huang, Y.B., Luo, F.J., Zhang, P., Zhang, C.C., Xu, M.H., Liu, J.C., Heng, Y.K., Yang, C.G., Jiang, X.S., Li, F., Ye, M.,

- Chen, H.S.: Comparison on PMT Waveform Reconstructions with JUNO Prototype. *JINST* **14**(08), 08002 (2019) <https://doi.org/10.1088/1748-0221/14/08/T08002>
- [11] Zhang, A., Xu, B., Weng, J., Chen, H., Shao, W., Xu, T., Ren, L., Qian, S., Wang, Z., Chen, S.: Performance evaluation of the 8-inch MCP-PMT for Jinping Neutrino Experiment. *Nuclear Instruments and Methods in Physics Research Section A: Accelerators, Spectrometers, Detectors and Associated Equipment* **1055**, 168506 (2023) <https://doi.org/10.1016/j.nima.2023.168506> . Accessed 2023-08-02
- [12] Xu, D.C., Xu, B.D., Bao, E.J., Wu, Y.Y., Zhang, A.Q., Wang, Y.Y., Zhang, G.L., Xu, Y., Guo, Z.Y., Pei, J.H., Mao, H.Y., Liu, J.S., Wang, Z., Chen, S.M.: Towards the ultimate PMT waveform analysis for neutrino and dark matter experiments. *Journal of Instrumentation* **17**(06), 06040 (2022) <https://doi.org/10.1088/1748-0221/17/06/P06040> . Publisher: IOP Publishing. Accessed 2022-09-18
- [13] Luo, X.L., Modamio, V., Nyberg, J., Valiente-Dobón, J.J., Nishada, Q., Angelis, G.d., Agramunt, J., Egea, F.J., Erduran, M.N., Ertürk, S., France, G.d., Gadea, A., González, V., Goasduff, A., Hüyük, T., Jaworski, G., Moszyński, M., Nitto, A.D., Palacz, M., Söderström, P.-A., Sanchis, E., Triossi, A., Wadsworth, R.: Pulse pile-up identification and reconstruction for liquid scintillator based neutron detectors. *Nuclear Instruments and Methods in Physics Research Section A: Accelerators, Spectrometers, Detectors and Associated Equipment* **897**, 59–65 (2018) <https://doi.org/10.1016/j.nima.2018.03.078>
- [14] Green, P.J.: Reversible jump markov chain monte carlo computation and bayesian model determination. *Biometrika* **82**(4), 711–732 (1995). Accessed 2023-11-25
- [15] Hastings, W.K.: Monte Carlo sampling methods using Markov chains and their applications. *Biometrika* **57**(1), 97–109 (1970) <https://doi.org/10.1093/biomet/57.1.97> . Accessed 2021-12-08
- [16] Bellamy, E.H., Bellettini, G., Budagov, J., Cervelli, F., Chirikov-Zorin, I., Incagli, M., Lucchesi, D., Pagliarone, C., Tokar, S., Zetti, F.: Absolute calibration and monitoring of a spectrometric channel using a photomultiplier. *Nuclear Instruments and Methods in Physics Research Section A: Accelerators, Spectrometers, Detectors and Associated Equipment* **339**(3), 468–476 (1994) [https://doi.org/10.1016/0168-9002\(94\)90183-X](https://doi.org/10.1016/0168-9002(94)90183-X) . Number: 3 00170. Accessed 2015-07-01
- [17] Stein, J., Kreuels, A., Kong, Y., Lentering, R., Ruhnau, K., Scherwinski, F., Wolf, A.: Experiment and modeling of scintillation photon-counting and current measurement for PMT gain stabilization. *Nuclear Instruments and Methods in Physics Research Section A: Accelerators, Spectrometers, Detectors and Associated Equipment* **782**, 20–27 (2015) <https://doi.org/10.1016/j.nima.2015.01.101>
- [18] Lombardi, P., Ortica, F., Ranucci, G., Romani, A.: Decay time and pulse shape

- discrimination of liquid scintillators based on novel solvents. *Nuclear Instruments and Methods in Physics Research Section A: Accelerators, Spectrometers, Detectors and Associated Equipment* **701**, 133–144 (2013) <https://doi.org/10.1016/j.nima.2012.10.061> . Accessed 2020-02-22
- [19] *Photomultiplier Tubes: Basics and Applications*, 4th edn. Hamamatsu Photonics (2017). 00126
- [20] Dossi, R., Ianni, A., Ranucci, G., Smirnov, O.J.: Methods for precise photoelectron counting with photomultipliers. *Nuclear Instruments and Methods in Physics Research Section A: Accelerators, Spectrometers, Detectors and Associated Equipment* **451**(3), 623–637 (2000) [https://doi.org/10.1016/S0168-9002\(00\)00337-5](https://doi.org/10.1016/S0168-9002(00)00337-5) . Accessed 2019-01-22
- [21] Lehmann, A., Böhm, M., Eyrich, W., Miehling, D., Pfaffinger, M., Stelter, S., Uhlig, F., Ali, A., Belias, A., Dzhygadlo, R., Gerhardt, A., Götzen, K., Kalicy, G., Krebs, M., Lehmann, D., Nerling, F., Patsyuk, M., Peters, K., Schepers, G., Schmitt, L., Schwarz, C., Schwiening, J., Traxler, M., Düren, M., Etzelmüller, E., Föhl, K., Hayrapetyan, A., Kreutzfeld, K., Merle, O., Rieke, J., Schmidt, M., Wasem, T., Achenbach, P., Cardinali, M., Hoek, M., Lauth, W., Schlimme, S., Sfienti, C., Thiel, M.: Lifetime of MCP-PMTs and other performance features. *Journal of Instrumentation* **13**(02), 02010–02010 (2018) <https://doi.org/10.1088/1748-0221/13/02/C02010> . Accessed 2023-05-22
- [22] Guo, L., Xin, L., Li, L., Gou, Y., Sai, X., Li, S., Liu, H., Xu, X., Liu, B., Gao, G., He, K., Zhang, M., Qu, Y., Xue, Y., Wang, X., Chen, P., Tian, J.: Effects of secondary electron emission yield properties on gain and timing performance of ALD-coated MCP. *Nuclear Instruments and Methods in Physics Research Section A: Accelerators, Spectrometers, Detectors and Associated Equipment* **1005**, 165369 (2021) <https://doi.org/10.1016/j.nima.2021.165369> . Accessed 2023-04-12
- [23] Weng, J., Zhang, A., Wu, Q., Ma, L., Xu, B., Qian, S., Wang, Z., Chen, S.: Single electron charge spectra of 8-inch MCP-PMTs coated by atomic layer deposition (2024)
- [24] Zhang, H.Q., Wang, Z.M., Luo, F.J., Yang, A.B., Wu, D.R., Li, Y.C., Qin, Z.H., Yang, C.G., Heng, Y.K., Wang, Y.F., Chen, H.S.: Gain and charge response of 20” MCP and dynode PMTs. *Journal of Instrumentation* **16**, 08009 (2021) <https://doi.org/10.1088/1748-0221/16/08/T08009> . ADS Bibcode: 2021JInst..16.8009Z. Accessed 2022-01-03
- [25] Huang, Y., Chang, J., Cheng, Y., Chen, Z., Hu, J., Ji, X., Li, F., Li, J., Li, Q., Qian, X., Jetter, S., Wang, W., Wang, Z., Xu, Y., Yu, Z.: The Flash ADC system and PMT waveform reconstruction for the Daya Bay experiment. *Nuclear Instruments and Methods in Physics Research Section A: Accelerators, Spectrometers, Detectors and Associated Equipment* **895**, 48–55 (2018) <https://doi.org/10.1016/j.nima.2018.03.061> . Accessed 2019-05-08

- [26] Grassi, M., Montuschi, M., Baldoncini, M., Mantovani, F., Ricci, B., Andronico, G., Antonelli, V., Bellato, M., E. Bernieri, A. Brigatti, Brugnera, R., Budano, A., Buscemi, M., Bussino, S., Caruso, R., Chiesa, D., Corti, D., Corso, F.D., Ding, X.F., Dusini, S., Fabbri, A., Fiorentini, G., Ford, R., Formozov, A., Galet, G., Garfagnini, A., M. Giammarchi, Giaz, A., Insolia, A., Isocrate, R., Lippi, I., Longhitano, F., Presti, D.L., Lombardi, P., F. Marini, Mari, S.M., Martellini, C., Meroni, E., Mezzetto, M., Miramonti, L., Monforte, S., Nastasi, M., F. Ortica, Paoloni, A., Parmeggiano, S., Pedretti, D., Pelliccia, N., Pompilio, R., Previtali, E., Ranucci, G., A.C. Re, Romani, A., Saggese, P., Salamanna, G., Sawy, F.H., Settanta, G., Sisti, M., Sirignano, C., Spinetti, M., L. Stanco, Strati, V., Verde, G., Votano, L.: Charge reconstruction in large-area photomultipliers. *Journal of Instrumentation* **13**(02), 02008 (2018) <https://doi.org/10.1088/1748-0221/13/02/P02008> . Accessed 2019-01-22
- [27] Jetter, S., Dwyer, D., Jiang, W.-Q., Liu, D.-W., Wang, Y.-F., Wang, Z.-M., Wen, L.-J.: PMT waveform modeling at the Daya Bay experiment. *Chinese Physics C* **36**(8), 733–741 (2012) <https://doi.org/10.1088/1674-1137/36/8/009> . Accessed 2019-05-08
- [28] Rosen, K.H.: *Discrete Mathematics and Its Applications*, 5th edn. McGraw-Hill Higher Education, USA (2002)
- [29] Geman, S., Geman, D.: Stochastic Relaxation, Gibbs Distributions, and the Bayesian Restoration of Images. *IEEE Transactions on Pattern Analysis and Machine Intelligence* **PAMI-6**(6), 721–741 (1984) <https://doi.org/10.1109/TPAMI.1984.4767596>
- [30] Lucy, L.B.: An iterative technique for the rectification of observed distributions. *The Astronomical Journal* **79**, 745 (1974) <https://doi.org/10.1086/111605> . Accessed 2019-04-18
- [31] Zhang, F., Yu, B., Hu, W., Yang, M., Cao, G., Cao, J., Zhou, L.: Measurement of the liquid scintillator nonlinear energy response to electron (2015). <http://hepnp.ihep.ac.cn/en/article/doi/10.1088/1674-1137/39/1/016003> Accessed 2019-03-01
- [32] Guo, Z., Yeh, M., Zhang, R., Cao, D.-W., Qi, M., Wang, Z., Chen, S.: Slow liquid scintillator candidates for MeV-scale neutrino experiments. *Astroparticle Physics* **109**, 33–40 (2019) <https://doi.org/10.1016/j.astropartphys.2019.02.001> . Accessed 2021-01-27
- [33] Dongarra, J., Hammarling, S., Higham, N.J., Relton, S.D., Valero-Lara, P., Zounon, M.: The design and performance of batched blas on modern high-performance computing systems. *Procedia Computer Science* **108**, 495–504 (2017) <https://doi.org/10.1016/j.procs.2017.05.138> . International Conference on Computational Science, ICCS 2017, 12-14 June 2017, Zurich, Switzerland
- [34] Harris, C.R., Millman, K.J., Walt, S.J., Gommers, R., Virtanen, P., Cournapeau,



- D., Wieser, E., Taylor, J., Berg, S., Smith, N.J., Kern, R., Picus, M., Hoyer, S., Kerkwijk, M.H., Brett, M., Haldane, A., R  o, J.F., Wiebe, M., Peterson, P., G  rard-Marchant, P., Sheppard, K., Reddy, T., Weckesser, W., Abbasi, H., Gohlke, C., Oliphant, T.E.: Array programming with NumPy. *Nature* **585**(7825), 357–362 (2020) <https://doi.org/10.1038/s41586-020-2649-2>
- [35] Okuta, R., Unno, Y., Nishino, D., Hido, S., Loomis, C.: Cupy: A numpy-compatible library for nvidia gpu calculations. In: Proceedings of Workshop on Machine Learning Systems (LearningSys) in The Thirty-first Annual Conference on Neural Information Processing Systems (NIPS) (2017). [http://learningsys.org/nips17/assets/papers/paper\\_16.pdf](http://learningsys.org/nips17/assets/papers/paper_16.pdf)
- [36] NVIDIA: Nvidia Tesla P100 GPU. Pascal Architecture White Paper **47** (2016)
- [37] Gelman, A., Rubin, D.: Inference from Iterative Simulation Using Multiple Sequences. *Statist. Sci* **7**(4) (1992)
- [38] Brooks, S., Gelman, A.: General Methods for Monitoring Convergence of Iterative Simulations. *Journal of Computational and Graphical Statistics* **7** (1998)
- [39] Villani, C.: The Wasserstein distances. In: Optimal Transport. Grundlehren der mathematischen Wissenschaften, pp. 93–111. Springer, Berlin, Heidelberg (2009)
- [40] Szydagis, M., Block, G.A., Farquhar, C., Flesher, A.J., Kozlova, E.S., Levy, C., Mangus, E.A., Mooney, M., Mueller, J., Rischbieter, G.R.C., Schwartz, A.K.: A Review of Basic Energy Reconstruction Techniques in Liquid Xenon and Argon Detectors for Dark Matter and Neutrino Physics Using NEST. *Instruments* **5**(1), 13 (2021) <https://doi.org/10.3390/instruments5010013> . Number: 1 Publisher: Multidisciplinary Digital Publishing Institute. Accessed 2022-07-03
- [41] Tipping, M.: The Relevance Vector Machine. In: Solla, S., Leen, T., M  ller, K. (eds.) *Advances in Neural Information Processing Systems*, vol. 12. MIT Press, USA (1999). [https://proceedings.neurips.cc/paper\\_files/paper/1999/file/f3144cefe89a60d6a1afaf7859c5076b-Paper.pdf](https://proceedings.neurips.cc/paper_files/paper/1999/file/f3144cefe89a60d6a1afaf7859c5076b-Paper.pdf)
- [42] Tipping, M.E.: Sparse Bayesian Learning and the Relevance Vector Machine. *Journal of Machine Learning Research* **1**, 211–244 (2001). Publisher: Journal of Machine Learning Research
- [43] Woodbury, M.A.: *Inverting Modified Matrices*. Princeton, NJ : Department of Statistics, Princeton University, USA (1950)